Preprints.org

Article

Not peer-reviewed version

High-Sensitivity and Temperature-Robust Gas Sensor Based on Magnetically Induced Differential Mode Splitting in InSb Photonic Crystals

Jin Zhang , Leyu Chen , Chenxi Xu , Haifeng Zhang *

Posted Date: 26 February 2026

doi: 10.20944/preprints202602.1579.v1

Keywords: magneto-optical photonic crystals; refractive index sensing; differential detection strategy; multi-objective dragonfly algorithm; indium antimonide; temperature robustness

Preprints.org is a free multidisciplinary platform providing preprint service that is dedicated to making early versions of research outputs permanently available and citable. Preprints posted at Preprints.org appear in Web of Science, Crossref, Google Scholar, Scilit, Europe PMC.

Copyright: This open access article is published under a Creative Commons CC BY 4.0 license, which permit the free download, distribution, and reuse, provided that the author and preprint are cited in any reuse.

Preprints.org (www.preprints.org) | NOT PEER-REVIEWED | Posted: 26 February 2026 doi:10.20944/preprints202602.1579.v1

Disclaimer/Publisher's Note: The statements, opinions, and data contained in all publications are solely those of the individual author(s) and contributor(s) and not of MDPI and/or the editor(s). MDPI and/or the editor(s) disclaim responsibility for any injury to people or property resulting from any ideas, methods, instructions, or products referred to in the content.

Article

High-Sensitivity and Temperature-Robust Gas Sensor Based on Magnetically Induced Differential Mode Splitting in InSb Photonic Crystals

Jin Zhang [1], Leyu Chen [1], Chenxi Xu [2] and Haifeng Zhang [1,2,*]

[1] College of Electronic Engineering, Tongda College of Nanjing University of Posts and Telecommunications , Yangzhou 225127, China

[2] College of Electronic and Optical Engineering & College of Flexible Electronics (Future Technology), Nanjing University of Posts and Telecommunications, Nanjing 210023, China

* Correspondence: hanlor@163.com or hanlor@njupt.edu.cn

Abstract

High-precision detection of hazardous gases with low refractive indices ranging from 1.000 to 1.100, specifically including methane, carbon monoxide, and sulfur dioxide, is critical for industrial safety, yet conventional sensors often suffer from limited sensitivity and severe thermal cross-sensitivity. This work presents a Magneto-Optical Differential Photonic Crystals Sensor (MO-DPCS) utilizing Indium Antimonide (InSb) to address these constraints. Employing the Multi-Objective Dragonfly Algorithm (MODA), the system was inversely optimized to maximize the magneto-optical polarization splitting while rigorously maintaining an ultra-high transmission efficiency. Crucially, an angular interrogation architecture operating under oblique incidence is established to maximize the magneto-optical non-reciprocity, where the detection is realized by fixing the terahertz source frequency and monitoring the precise angular displacements of the steep spectral edges. A differential detection technique was employed to utilize the non-reciprocal phase changes wherein Transverse Electric (TE) and Transverse Magnetic (TM) modes display contrasting kinematic characteristics in the presence of an external magnetic field. The findings indicate that with an adjusted magnetic field of 0.033 T, the MO-DPCS attains an exceptional differential sensitivity of 30.8 °/RIU, much above the 0.8 °/RIU seen in the unmagnetized condition. The differential approach efficiently eliminates common-mode thermal noise, minimizing temperature-induced drift to below 0.35° across a 1 K range. The suggested MO-DPCS offers a robust, self-referencing solution for stable and high-sensitivity gas sensing applications with a detection limit of 4.18×10^{-4} RIU.

Keywords: magneto-optical photonic crystals; refractive index sensing; differential detection strategy; multi-objective dragonfly algorithm; indium antimonide; temperature robustness

1. Introduction

The accurate identification of dangerous gases is a crucial issue in chemical engineering and environmental safety [1,2]. Specifically, common hazardous industrial gases such as methane (CH_4), carbon monoxide (CO), and nitrogen oxides (NO_x) exhibit extremely low refractive indices, typically ranging from 1.0003 to 1.0008 at standard atmospheric pressure. The release or accumulation of these flammable, explosive, or poisonous volatile organic compounds presents significant hazards to industrial infrastructure and public health. However, the fluctuation in gas concentration is inherently linked to minute changes in the refractive index of the medium, often on the magnitude of 10^{-4} to 10^{-5} RIU. This necessitates sensing devices with an exceptionally low Limit of Detection (*LOD*) to distinguish target analytes from the background environment. Consequently, optical refractive index sensing has emerged as an indispensable technology in chemical analysis [3,4], biosensing [5,6], new energy monitoring [7,8], and environmental governance [9,10]. Utilizing

© 2025 by the author(s). Distributed under a Creative Commons CC BY license.

Preprints.org (www.preprints.org) | NOT PEER-REVIEWED | Posted: 26 February 2026 doi:10.20944/preprints202602.1579.v1

benefits such as non-contact measurement, rapid response, high precision, and resistance to electromagnetic interference, optical sensors have emerged as the predominant method for detection [11–14]. A variety of sensing designs has been developed, including total internal reflection techniques [15,16], surface plasmon resonance [17,18], interferometry [19,20], and fiber-optic sensing [21–23]. Notwithstanding the compactness and stability of these conventional designs, numerous contemporary systems continue to be hindered by restricted resolution and poor quality factors (Q) [24,25]. This constraint necessarily results in inadequate sensitivity and a heightened chance of false negatives or overlooked detection in practical applications [26,27]. With the progression of the Internet of things and intelligent manufacturing [28], the necessity for sensors that overcome performance limitations has become critical.

To tackle these issues, one-dimensional photonic crystals (1D PCs) [29–32] have attracted considerable interest as a viable sensing platform owing to their great integration ease and relatively straightforward fabrication methods. Recent improvements have enhanced the performance of PCs significantly. In 2024, Qi *et al*. [33] attained angle-insensitive ultra-high-Q resonances by integrating bound states in the continuum, developing a hypersensitive environmental refractive index sensor and a temperature sensor with maximum sensitivities of 8.67×10^5 μm/RIU and 2.8×10^6 μm/°C, respectively. While this work achieved an impressive detection limit approximately 10^{-5} RIU within the gaseous refractive index range, it primarily relies on wavelength interrogation, which inherently necessitates high-resolution spectrometers, thereby increasing the system complexity and cost. In 2025, Li *et al*. [34] introduced a Ω-shaped sensor utilizing Gold Nanoparticles/Polydimethylsiloxane (AuNPs/PDMS) core-shell structures for the concurrent measurement of refractive index and temperature. Despite these advancements in spectral detection, angular interrogation techniques have emerged as a robust alternative for constructing compact and cost-effective sensing systems. By fixing the excitation frequency and monitoring the angular shift of resonance modes, angular sensors eliminate the need for bulky spectral analyzers. Currently, high-performance angular sensing is predominantly realized through Surface Plasmon Resonance (SPR) or defect-mode PCs. However, most existing angular sensors employ passive measurement schemes that track absolute angular shifts, leaving them susceptible to source fluctuations and environmental noise. Therefore, developing an active angular sensing architecture that incorporates differential detection capabilities is critical for further improving measurement stability and resolution. To enhance sensing capabilities from passive detection to active tunable sensing, semiconductor materials are progressively incorporated into dielectric stacks. Indium antimonide (InSb) is a remarkable candidate for the terahertz (THz) spectrum [35,36]. InSb is distinguished by its exceptionally low effective electron mass and elevated carrier mobility, resulting in a significant magneto-optical effect [37]. In the presence of an external magnetic field, permittivity transforms into a tensor facilitating the non-reciprocal manipulation of light, which is a capability absent in passive dielectrics [38]. To further optimize the structural performance, porous silica (porous SiO_2) is utilized as the low-refractive-index material [39,40]. Porous SiO_2 represents the most mature and technologically established solution for achieving extremely low refractive indices, which is essential for maximizing the refractive index contrast and enhancing the optical field confinement within the device.

The design of high-performance magneto-optical devices constitutes a complicated multiparametric challenge. Conventional design methodologies frequently depend on trial-and-error or empirical intuition, resulting in inefficiency and a tendency to achieve only local optima. The recent surge in Artificial Intelligence (AI) research has facilitated the integration of intelligent algorithms with nanophotonics, leading to novel opportunities for device optimization [41,42]. In the realm of optical sensing and perception, meta-heuristic algorithms such as Genetic Algorithms and Particle Swarm Optimization have been extensively applied to solve inverse design problems, enabling the precise tailoring of geometric parameters for enhanced light-matter interaction. For instance, in 2023, Teng *et al*. [43] significantly enhanced the performance of surface plasmon resonance sensors in a Kretschmann structure through genetic algorithms, exhibiting anti-crossing behavior and achieving an unprecedented sensitivity of 1364 °/RIU. However, traditional algorithms often struggle with

© 2025 by the author(s). Distributed under a Creative Commons CC BY license.

Preprints.org (www.preprints.org) | NOT PEER-REVIEWED | Posted: 26 February 2026 doi:10.20944/preprints202602.1579.v1

premature convergence when navigating the high-dimensional search spaces of complex multilayer structures. To execute the inverse design of the sensor architecture in this study, the Multi-Objective Dragonfly Algorithm (MODA) was employed, which was first proposed by Mirjalili in 2015 [44]. Distinct from standard evolutionary algorithms, MODA is characterized by its unique ability to switch between static (exploitation) and dynamic (exploration) swarming behaviors. The core inspiration stems from the natural hunting and migration mechanisms of dragonflies, by dynamically adjusting weights for separation, alignment, and cohesion, MODA effectively maintains population diversity to avoid local optima while ensuring rapid convergence towards the Pareto front. This capability makes it uniquely suited for simultaneously optimizing conflicting objectives, such as maximizing the Rectangular Coefficient (*RC*) [45] while maintaining fabrication feasibility. Through this computational optimization of layer thicknesses, a resonance mode exhibiting an exceptionally high *RC* is attained. This guarantees a spectral profile characterized by a steep and virtually vertical band edge, establishing the physical basis for high-sensitivity detection that manual tuning cannot readily achieve.

Notwithstanding these breakthroughs, a significant gap persists in current sensing methodologies. Most existing refractive index sensors rely heavily on wavelength interrogation, which necessitates bulky and expensive spectral analyzers, or depend on the absolute angular shift of a single resonance peak, leaving them vulnerable to source fluctuations and environmental noise. To address these restrictions, this work introduces a novel Magneto-Optical Differential Photonic Crystals Sensor (MO-DPCS) based on a precise angular interrogation architecture. Unlike intricate lithographic structures, the approach preserves a straightforward multilayered arrangement while implementing a differential angular detection strategy [46–48]. The sensing mechanism is fundamentally rooted in the magneto-optical non-reciprocity of the InSb material. Under an external magnetic field, the gyrotropic permittivity of InSb breaks the time-reversal symmetry, causing the dispersion relations of Transverse Electric (TE) and Transverse Magnetic (TM) modes to split. Consequently, at a fixed THz frequency, the photonic bandgap edges of the two modes exhibit distinct angular cutoff characteristics. By utilizing the angular difference ($\Delta\theta$) between the TE and TM modes as the sensing signal, this method not only doubles the interrogation efficiency but also efficiently mitigates common-mode noise such as thermal drift and mechanical vibrations. This greatly improves the resolution and stability of the sensor in intricate sensing situations.

2. Configuration and Methods

The proposed MO-DPCS is engineered as a one-dimensional multilayered structure specifically for the detection of hazardous gases with low refractive indices, such as CH_4, CO, and sulfur dioxide (SO_2). The design focuses on a refractive index spectrum ranging from 1.000 to 1.100. This interval is strategically selected to strictly encompass the refractive indices of vacuum (n = 1.0), atmospheric air (n ≈ 1.0003), and the majority of industrial volatile gases, ensuring comprehensive coverage for gas leakage monitoring. This apparatus attains enhanced sensitivity (*S*) via a differential sensing methodology. Figure 1 demonstrates that the structure operates as a magneto-optical Fabry-Pérot cavity [49], consisting of a core host structure situated between two symmetrical anti-reflection structures (AFSs) [50]. The fundamental host structure comprises a singular layer of InSb with an optimized thickness d_H of 433.7464 μm, leveraging the epsilon-near-zero (ENZ) [51,52] property to stimulate a designated angular transmission window (ATW). To reduce signal attenuation caused by thin-film resonance effects at energy transition points, the host structure is interposed between two identical AFSs designed using impedance matching to minimize reflection losses [53,54]. Each AFS consists of 7 periods of alternating layers of InSb, with a thickness of d_a = 7.3047 μm, and porous SiO_2 layers, with a thickness of d_b = 1.442 μm. The porous SiO_2 is chosen for its steady low refractive index and a regulated dielectric constant of 1.50. A key aspect of this design is the synchronized modulation of the InSb layers within both the host structure and the AFSs. The device is exposed to an incoming electromagnetic wave (EW) characterized by a wave vector *k*, which propagates in the *xoz*-plane (the plane of incidence) at an incidence angle θ. An external static magnetic field *B* is oriented along the

© 2025 by the author(s). Distributed under a Creative Commons CC BY license.

Preprints.org (www.preprints.org) | NOT PEER-REVIEWED | Posted: 26 February 2026 doi:10.20944/preprints202602.1579.v1

positive +*y*-axis, maintaining a direction perpendicular to the plane of incidence to establish the Voigt configuration [55]. Under this geometric arrangement, the incident light is decomposed into two orthogonal polarization modes. In the TE wave, the electric field vector *E* oscillates parallel to the +*y*-axis and is thus aligned with *B*. Conversely, in the TM wave, the magnetic field vector *H* oscillates parallel to the +*y*-axis, which constrains the electric field vector *E* to lie within the *xoz*-plane and remain perpendicular to the direction of *B*. This configuration generates a significant non-reciprocal magneto-optical effect specifically for the TM mode while maintaining the TE mode as a quasi-static reference, thereby providing the MO-DPCS with enhanced anti-interference capabilities against environmental variations and improved detection resolution by effectively mitigating common-mode noise [56].

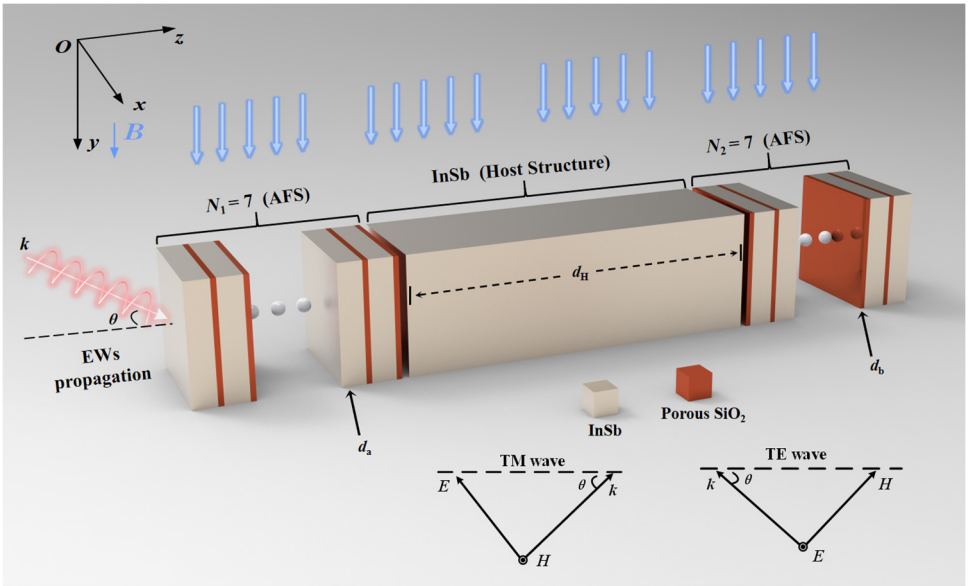

Figure 1. Schematic diagram of the designed sensor MO-DPCS. The host structure is composed of a single layer of InSb material while the AFSs on both sides are periodic structures consisting of alternating InSb and porous SiO_2. The blue arrows explicitly indicate the direction of the external static magnetic field *B*, which is applied along the positive +*y*-axis (perpendicular to the plane of incidence) to establish the Voigt configuration.

The permittivity of InSb can be expressed in tensor form [57]:

$$\varepsilon_i = \begin{bmatrix} \varepsilon_x & 0 & i\varepsilon_{xz} \\ 0 & \varepsilon_y & 0 \\ -i\varepsilon_{xz} & 0 & \varepsilon_x \end{bmatrix} \tag{1a}$$

$$\varepsilon_x = \varepsilon_\infty - \varepsilon_\infty \frac{\omega_p^2(\omega + i\gamma)}{\omega\left[(\omega + i\gamma)^2 - \omega_c^2\right]} \tag{1b}$$

$$\varepsilon_y = \varepsilon_\infty - \varepsilon_\infty \frac{\omega_p^2}{\omega(\omega + i\gamma)} \tag{1c}$$

$$\varepsilon_{xz} = \varepsilon_\infty \frac{\omega_p^2 \omega_c}{\omega\left[(\omega + i\gamma)^2 - \omega_c^2\right]} \tag{1d}$$

In this context, ε_∞ denotes the high-frequency dielectric constant of InSb, γ signifies the carrier collision frequency [57], *m* and *e* correspond to the mass and charge of an electron, respectively, and

© 2025 by the author(s). Distributed under a Creative Commons CC BY license.

Preprints.org (www.preprints.org) | NOT PEER-REVIEWED | Posted: 26 February 2026 doi:10.20944/preprints202602.1579.v1

m^* equals 0.015m, indicating the effective mass of the carriers. ω_p is the plasma frequency, defined as $(Ne/\varepsilon_0\varepsilon_\infty m^*)^{1/2}$. Here, ε_0 represents vacuum permittivity, while ambient temperature is denoted by T_0. N is specified as [57]:

$$N\left(cm^{-3}\right)=5.76\times10^{14}T_0^{1.5}\times e^{\left(\frac{-0.26}{2\times8.625\times10^{-5}\times T_0}\right)} \tag{2}$$

The effective dielectric constant for an incident plane electromagnetic wave in TE mode can be expressed as [57]:

$$\varepsilon_{\mathrm{TE}}=\varepsilon_\infty\left(1-\frac{\omega_p^2}{\omega(\omega+i\gamma)}\right) \tag{3}$$

In the Voigt configuration, an external magnetic field B is applied perpendicularly to the wave propagation direction, resulting in an anisotropic dielectric response of InSb. In TE mode, the electric field oscillates parallel to B, resulting in carrier motion being unaffected by the Lorentz force. Thus, the effective refractive index for TE mode is isotropic, represented as $n_a(\mathrm{TE})=(\varepsilon_{\mathrm{TE}})^{1/2}$ [58]. Conversely, the TM mode exhibits an electric field orthogonal to B, resulting in robust coupling between the EWs and free carriers influenced by the Lorentz force. This interaction is defined by the cyclotron frequency $\omega_c = eB/m^*$ [57], and the effective refractive index in this mode is given by $n_a(\mathrm{TM}) = [(\varepsilon_x - \varepsilon_{xz})/\varepsilon_x]^{1/2}$ [59].

Owing to these distinct dielectric responses, the TE mode remains isotropic, whereas the TM mode becomes magneto-optically anisotropic under the influence of the Lorentz force. This divergence in propagation characteristics dictates that, within a periodically layered medium, the characteristic transfer matrix of each layer must be formulated independently for the TM and TE waves, which are respectively expressed as[60,61]:

$$\boldsymbol{M}_n=\begin{bmatrix}\cos\delta_n & -ip_n^{-1}\sin\delta_n\\ -ip_n\sin\delta_n & \cos\delta_n\end{bmatrix} \tag{4a}$$

$$\boldsymbol{M}_{\mathrm{TM}}=\begin{bmatrix}\cos\left(k_{1z}d_{\mathrm{n}}\right)+\dfrac{k_{1x}\boldsymbol{\varepsilon}_{xz}}{k_{1z}\boldsymbol{\varepsilon}_{xx}}\sin\left(k_{1z}d_{\mathrm{n}}\right) & -ip_1^{-1}\sin\left(k_{1z}d_{\mathrm{n}}\right)\\ -ip_1\sin\left(k_{1z}d_{\mathrm{n}}\right) & \cos\left(k_{1z}d_{\mathrm{n}}\right)-\dfrac{k_{1x}\boldsymbol{\varepsilon}_{xz}}{k_{1z}\boldsymbol{\varepsilon}_{xx}}\sin\left(k_{1z}d_{\mathrm{n}}\right)\end{bmatrix} \tag{4b}$$

$$\boldsymbol{M}_{\mathrm{TE}}=\begin{bmatrix}\cos\left(k_{2z}d_{\mathrm{n}}\right) & -ip_2^{-1}\sin\left(k_{2z}d_{\mathrm{n}}\right)\\ -ip_2\sin\left(k_{2z}d_{\mathrm{n}}\right) & \cos\left(k_{2z}d_{\mathrm{n}}\right)\end{bmatrix} \tag{4c}$$

where $k_{iz} = k_i\cos\theta_i = (\omega/c)n_i\cos\theta_i$, $k_{1x} = k_1\sin\theta_i$, $p_i = (\varepsilon_0/\mu_0)^{1/2}n_i\cos\theta_i$, $\varepsilon_0 = 8.8542\times10^{-12}$ is the vacuum dielectric constant, and $\mu_0 = 4\pi\times10^{-7}$ is the permeability of vacuum [59]. To thoroughly examine the optical transmission characteristics of the proposed MO-DPCS, the equations of Maxwell were resolved utilising the transfer matrix method (TMM) [60,61] under the continuity boundary conditions for tangential electric and magnetic fields. Let $\boldsymbol{M}_a$ represent the characteristic matrix of the InSb material within the AFSs structure, $\boldsymbol{M}_b$ represent the characteristic matrix of the porous SiO_2 within the AFSs structure, and $\boldsymbol{M}_H$ represent the characteristic matrix of the host structure. The TMM can be employed to calculate energy transfer between dielectric layers.

$$\boldsymbol{M}=\begin{bmatrix}\boldsymbol{M}_{11} & \boldsymbol{M}_{12}\\ \boldsymbol{M}_{21} & \boldsymbol{M}_{22}\end{bmatrix}=\left(\boldsymbol{M}_{\mathrm{a}}\boldsymbol{M}_{\mathrm{b}}\right)^7\boldsymbol{M}_{\mathrm{H}}\left(\boldsymbol{M}_{\mathrm{b}}\boldsymbol{M}_{\mathrm{a}}\right)^7 \tag{5}$$

The transmission coefficient t can be articulated using the subsequent formula [62]:

© 2025 by the author(s). Distributed under a Creative Commons CC BY license.

Preprints.org (www.preprints.org) | NOT PEER-REVIEWED | Posted: 26 February 2026 doi:10.20944/preprints202602.1579.v1

$$t = \left| \frac{2p_0}{\left(\boldsymbol{M}_{11} + \boldsymbol{M}_{12}p_0\right)p_0 + \left(\boldsymbol{M}_{21} + \boldsymbol{M}_{22}p_0\right)} \right| \tag{6}$$

The transmittance T can be articulated as [62]:

$$T = |t|^2 \tag{7}$$

3. Results

3.1. Spectral Characteristics and Algorithm-Driven Optimization of Magneto-Optical Polarization

The optical transmission properties of the proposed MO-DPCS were initially examined to confirm its efficacy as a high-performance angular filter. Figure 2 illustrates that the periodic stratification of the structure results in a pronounced photonic band gap (PBG) [63,64] attributable to Bragg interference [65]. The MO-DPCS demonstrates an exceptional ATW for both TE and TM waves inside the passband. The transmission efficiency typically surpasses 0.9 across the operational angular range, guaranteeing adequate signal intensity for reliable detection even in lossy experimental conditions. The steepness of the transmission band edge is a crucial characteristic for ensuring excellent detection resolution [45]. A steeper edge indicates a more acute angular transition from the passband to the stopband, hence reducing the ambiguity in identifying the cutoff angle θ_{cutoff} and improving the *LOD*. The *RC* is employed as a statistic to quantify the sharpness of the band edge. The *RC* is delineated as [45]:

$$RC = \frac{\Delta\theta_{-3\mathrm{dB}}}{\Delta\theta_{-30\mathrm{dB}}} \tag{8}$$

$\Delta\theta_{\text{-3dB}}$ and $\Delta\theta_{\text{-30dB}}$ represent the angular widths recorded at -3 dB with T = 0.5 and at -30 dB with T = 0.001, respectively. The rectangular coefficient varies from 0 to 1, with values approaching unity signifying a sharper band edge, therefore indicating more angular selectivity and greater measurement precision.

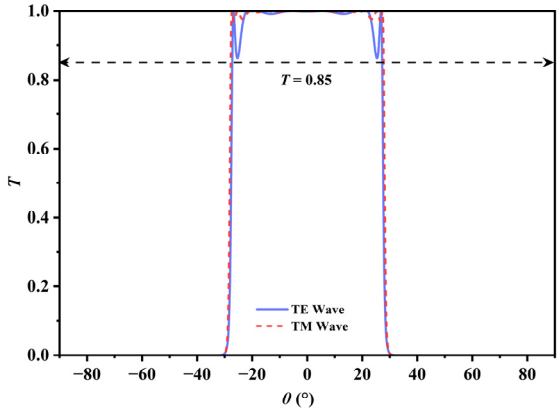

Figure 2. Angular transmission spectra of the MO-DPCS for TE and TM waves calculated at an operating frequency of 1.95 THz under a zero external magnetic field condition.

Figure 3 presents a quantitative evaluation regarding the spectral quality of the proposed sensor. Observations indicate that the *RC* values for both TE and TM modes remain consistently above 0.975 across the complete refractive index detection range from 1.000 to 1.100. Simultaneously, the device exhibits exceptional optical throughput, with the peak transmittance of the Angular Transmission Window (ATW) exceeding 99%. This persistently high *RC* indicates a nearly vertical band-edge profile, which is mathematically correlated with a minimized width of the transition region.

© 2025 by the author(s). Distributed under a Creative Commons CC BY license.

Preprints.org (www.preprints.org) | NOT PEER-REVIEWED | Posted: 26 February 2026 doi:10.20944/preprints202602.1579.v1

Physically, this "flat-top and steep-edge" spectral characteristic offers significant advantages, the high transmission efficiency markedly improves the Signal-to-Noise Ratio (SNR) of the detection system, ensuring that the cutoff point remains distinct even under weak signal conditions, while the high *RC* directly constrains the Full Width at Half Maximum (*FWHM*) of the resonance edge [25]. As a critical parameter for defining spectral resolution, the minimization of *FWHM* is the primary mechanism for maximizing the Figure of Merit (*FOM*). Consequently, the *FOM*—where higher values indicate superior quality—serves as the most equitable benchmark for evaluating the comprehensive performance of the sensor in practical applications. Although high-*Q* transmission is crucial, the implementation of differential detection requires divergent optical characteristics for TE and TM modes. In absence of an external magnetic field (B = 0 T), InSb functions as an isotropic material. Under these circumstances, the transmission spectra for TE and TM modes are essentially indistinguishable, with the cutoff angles θ_{TE} and θ_{TM} approximately coinciding. Thus, any environmental fluctuation would cause simultaneous shifts in both modes, leading to an insignificant differential signal where $\Delta\theta \approx 0$. To address this issue, a static magnetic field of 0.033 T is employed in the Voigt configuration. This field effectively disrupts the time-reversal symmetry of the system and induces gyrotropic anisotropy in the InSb layers. Crucially, the Lorentz force exerts a selective influence, it specifically modifies the effective refractive index of the TM mode, where the electric field vector *E* is orthogonal to the magnetic field vector *B*. In contrast, the TE mode, with *E* aligned parallel to *B*, remains predominantly unaffected. This magneto-optical polarization splitting generates two distinct signal channels within a single physical structure, creating the necessary bias for the ensuing differential detection technique.

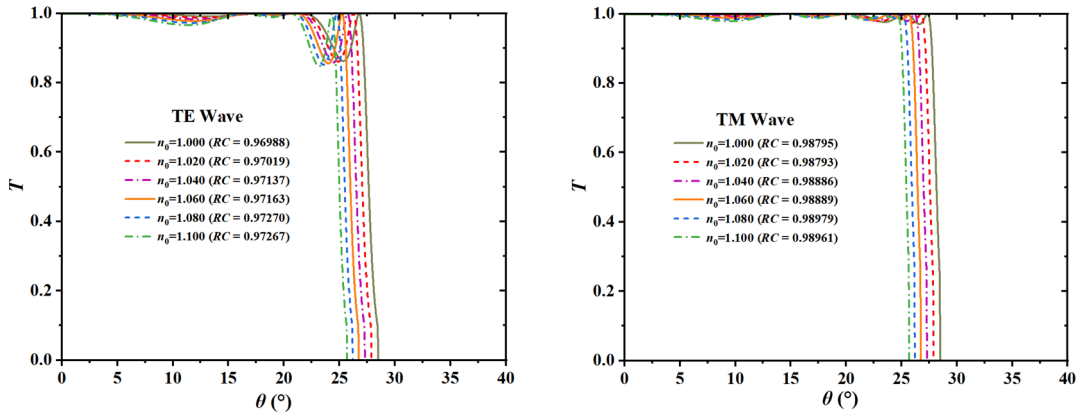

(**a**) (**b**)

Figure 3. Calculated angular transmission spectra along with the corresponding *RC* values for the MO-DPCS operating at a frequency of 1.95 THz. (a) Transmission spectra and *RC* values for the TE mode under varying background refractive indices ranging from 1.000 to 1.100; (b) Transmission spectra and *RC* values for the TM mode under the identical refractive index range. The numerical data within the legends indicate that the *RC* remains consistently high, exceeding 0.970 for the TE mode and 0.988 for the TM mode across the entire detection range, thereby demonstrating the superior steepness of the band edge and the structural foundation for high-precision sensing.

The MODA, a bio-inspired metaheuristic first proposed by Mirjalili in 2015 [44], was utilized to accurately ascertain the ideal magnetic field strength *B* that maximizes the polarization splitting effect while maintaining a high transmission efficiency of the TM mode. MODA epitomizes a leading edge in contemporary artificial intelligence research, distinguished by its unique mechanism that mimics the static and dynamic swarming behaviors of dragonflies. In the static phase (exploration), dragonflies form sub-groups to fly over different areas, which allows the algorithm to effectively avoid local optima. Conversely, in the dynamic phase (exploitation), the swarm migrates in a common direction, facilitating rapid convergence toward the global optimum. The core of this

© 2025 by the author(s). Distributed under a Creative Commons CC BY license.

Preprints.org (www.preprints.org) | NOT PEER-REVIEWED | Posted: 26 February 2026 doi:10.20944/preprints202602.1579.v1

algorithm is to calculate the step vectors and position vectors of dragonflies, which are shown as follows, representing their movement directions ΔX_i and positions X_i [44]. The detailed variable explanations are provided in Table 1 pseudo-code.

$$\Delta \boldsymbol{X}_{i+1} = \left(s\boldsymbol{S}_i + a\boldsymbol{A}_i + c\boldsymbol{C}_i + f\boldsymbol{F}_i + e\boldsymbol{E}_i\right) + w\Delta \boldsymbol{X}_i \tag{9a}$$

$$\boldsymbol{X}_{i+1} = \boldsymbol{X}_i + \Delta \boldsymbol{X}_{i+1} \tag{9b}$$

This exceptional capacity to balance exploration and exploitation makes MODA particularly suitable for addressing intricate, multi-variable engineering challenges with conflicting aims. The efficacy of such AI-driven optimization techniques has been extensively validated in the design of high-performance nanophotonic devices. For instance, Genetic Algorithms have been employed to develop ultra-sensitive SPR sensors, including a generic optimization technique that identified a series of sensors with sensitivity improvements of approximately 100%. Notably, a dual-mode SPR structure coupling Surface Plasmon Polaritons and waveguide modes in germanium dioxide was achieved, exhibiting anti-crossing behavior and an unprecedented sensitivity of 1364 °/RIU [43]. Other GA-optimized designs include bimetallic Al/Ag structures sandwiched in hBN (578 °/RIU at 633 nm) and hybrid hBN/MoS_2/hBN structures (676 °/RIU at 785 nm). Furthermore, deep learning approaches such as Convolutional Neural Networks (CNNs) have proven superior to traditional methods in the inverse design of Photonic Crystal Waveguides (PCWs). Hybrid frameworks combining the Grey Wolf Optimizer (GWO) with CNNs have also been utilized to optimize complex D-shaped photonic crystal fiber polarization filters, achieving a crosstalk of 965.3 dB and high confinement losses [42]. These cases underscore the powerful potential of intelligent algorithms in pushing the performance boundaries of photonic sensors. In this study, the optimization focused on a highly refined search space, as the requisite magnetic field adjustments are extremely subtle yet decisive for the resolution of the sensor. The algorithm was assigned the duty of navigating this delicate trade-off to determine a specific magnetic field intensity that maximizes the divergence between TE and TM modes while specifically maintaining a high transmission rate. Through rigorous iterative optimization, a magnetic field of 0.032 T was determined to be the global optimum. Figure 4 illustrates the optical response of the structure under optimal conditions, showcasing significant polarization separation while maintaining TM passband transmission above 0.9 (with a maximum transmissivity reaching 0.99). The detailed implementation logic and the mathematical foundation of the optimization technique are encapsulated in the pseudo-code provided in Table 1.

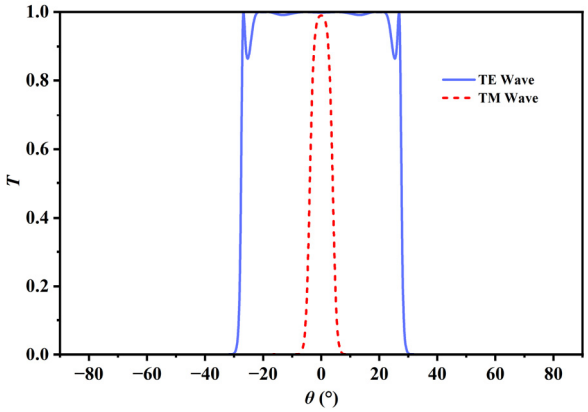

Figure 4. Optimized angular transmission spectra of the MO-DPCS for TE and TM modes calculated at an operating frequency of 1.95 THz under an optimized external magnetic field of 0.032 T obtained via the MODA. The blue and red curves correspond to the TE and TM modes, respectively. The plot visually demonstrates the achieved polarization splitting, thereby validating the effectiveness of the optimization strategy in balancing mode separation with signal integrity.

© 2025 by the author(s). Distributed under a Creative Commons CC BY license.

Preprints.org (www.preprints.org) | NOT PEER-REVIEWED | Posted: 26 February 2026 doi:10.20944/preprints202602.1579.v1

Table 1. MODA pseudo-code diagram.

Algorithm: Multi-Objective Dragonfly Algorithm for Magnetic Field Optimization

Initialize population:

for $i = 1$ *to* N **do**

| Magnetic field range: $\boldsymbol{X}_i$ = range(B_{min}, B_{max}) // Magnetic field initialization

end

Archive is empty

Iteration M**:**

for $n = 1$ *to* M_{max} **do**

| **Update** adaptive parameters: w, s, a, c, f and e // Update Pareto

| **Update** archive and select food/enemy position // Minimize objectives

| **for** $i = 1$ *to* N **do**

| | Separation: $\boldsymbol{S}_i \leftarrow$ -sum($\boldsymbol{X}_j$) - $\boldsymbol{X}_j$ // Update positions

| | Alignment: $\boldsymbol{A}_i \leftarrow$ mean($\Delta\boldsymbol{X}_j$)

| | Cohesion: $\boldsymbol{C}_i \leftarrow$ mean($\boldsymbol{X}_j$) - $\boldsymbol{X}_i$

| | Food: $\boldsymbol{F}_i \leftarrow$ Food position - $\boldsymbol{X}_i$

| | Enemy: $\boldsymbol{E}_i \leftarrow$ Enemy position + $\boldsymbol{X}_i$

| | **Calculate** step vectors and position vectors

| | $\Delta\boldsymbol{X}_{i+1} = s\times\boldsymbol{S}_i + a\times\boldsymbol{A}_i + c\times\boldsymbol{C}_i + f\times\boldsymbol{F}_i + e\times\boldsymbol{E}_i + w\times\Delta\boldsymbol{X}_i$

| | $\boldsymbol{X}_{i+1} = \boldsymbol{X}_i + \Delta\boldsymbol{X}_{i+1}$

| | **Update results**

| **end**

end

return Archive_X, Archive_F // Output results

To comprehensively execute the inverse design and ensure the rigorous coupling between the meta-heuristic optimization and the transfer matrix method calculations, the initial parameters of the MODA were meticulously configured. The optimization framework is multifaceted, encompassing global algorithmic settings, dynamically adaptive swarming coefficients, and strict electrodynamic constraints. Notably, the swarming parameters, such as separation, alignment, and cohesion weights, are non-static and adaptively transition from the exploration phase to the exploitation phase as iterations progress. Furthermore, the objective functions are evaluated under high-resolution angular interrogations and strictly bounded by intrinsic physical properties. The complete architectural parameters and boundary conditions governing this complex optimization process are systematically detailed in Table 2.

Table 2. MODA optimization parameters.

Category	Parameter	Description	Value/Range
I. Global Algorithmic Configurations	N	Population size	30
	M_{max}	Maximum iterations	50
	$N_{archive}$	Maximum capacity of Pareto archive	100
II. Dynamic Swarming Dynamics	r	Dynamic neighborhood radius	Non-linear expansion: $0.25\Delta \rightarrow 2.25\Delta$

© 2025 by the author(s). Distributed under a Creative Commons CC BY license.

Preprints.org (www.preprints.org) | NOT PEER-REVIEWED | Posted: 26 February 2026 doi:10.20944/preprints202602.1579.v1

	s, *a*, *c*	Separation, Alignment, and Cohesion factors	Adaptive decay proportional to 1/*M*
	f, *e*	Food attraction, and Enemy distraction	Stochastic and iteration-dependence
III. Physical Boundaries & Objective Functions	B_{search}	Search space for external magnetic field	0.001 ~ 0.0035 (T)
	θ_{scan}	Angular interrogation range and resolution	-90°~90°
	Obj_1	Primary objective function	Min{-(*Count*TE - *Count*TM)}
	Obj_2	Secondary objective function	Min{-*Count*TE}

3.2. Refractive Index Sensing Response and Sensitivity Analysis

The primary sensing mechanism of the proposed MO-DPCS relies on the dependence of PBG edge on the dielectric surroundings. Variations in the target gas concentration cause fluctuations in the background refractive index n_0, which subsequently modify the effective optical path length within the crystal layers. This alteration in the Bragg resonance condition results in a notable angular displacement of the transmission window edge. To clarify the precise effect of magnetic modulation, the response without an external magnetic field B = 0T was initially analyzed to establish a baseline. Specifically, Figure 5(a) and Figure 5(b) illustrate the transmission spectra for the TE and TM modes, respectively, demonstrating a concurrent trend towards reduced incidence angles as the refractive index increases from 1.000 to 1.100. While this synchronous blue-shift is characteristic of the unmagnetized state, the application of the optimal external magnetic field induces a distinct magneto-optical phenomenon. Under these magnetized conditions, the two orthogonal polarizations demonstrate contrasting shifting tendencies. The cutoff angle of the TE mode progressively decreases, whereas the cutoff angle of the TM mode shifts in the opposite direction and increases.

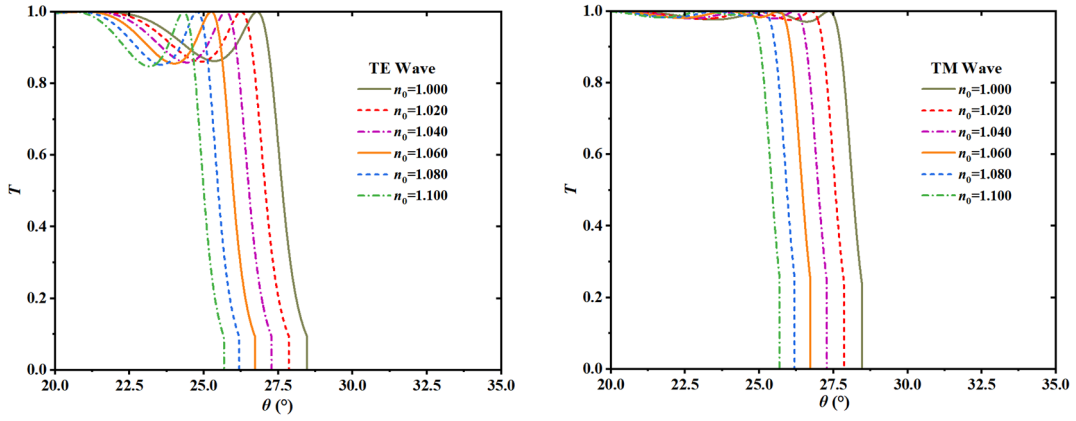

(**a**) (**b**)

Figure 5. Angular transmission spectra of the sensor calculated at an operating frequency of 1.95 THz in the absence of an external magnetic field where B is 0 T. (a) Transmission response for the TE mode as the background refractive index varies from 1.000 to 1.100; (b) Transmission response for the TM mode under the identical refractive index range. The observed synchronous shift of both modes towards smaller incident angles signifies the conventional baseline response of the structure prior to magnetic modulation.

The sensitivity, denoted as S, was computed for both modes and is fundamentally defined as the slope of the angular shift in relation to the change in refractive index. As depicted in Figure 6(a), in the unmagnetized state, both modes exhibit a highly similar synchronous response. The TE mode follows the linear equation θ_{cutoff} = -26.42n_0 + 54.03 ° with a correlation coefficient (R^2) of 0.99910, yielding a sensitivity θ_{TE} of -26.42 °/RIU. Concurrently, the TM mode is described by θ_{cutoff} = -27.22n_0 - 55.34 ° (R^2 = 0.99901), resulting in a sensitivity θ_{TM} of -27.22 °/RIU. Upon the application of the optimized external magnetic field, as shown in Figure 6(b), the two orthogonal polarizations

© 2025 by the author(s). Distributed under a Creative Commons CC BY license.

Preprints.org (www.preprints.org) | NOT PEER-REVIEWED | Posted: 26 February 2026 doi:10.20944/preprints202602.1579.v1

demonstrate contrasting shifting tendencies. The TE mode, remaining unaffected by the magnetic field, maintains its negative angular shift trend with θ_{TE} = -26.42 °/RIU. Conversely, the TM mode experiences strong Lorentz force coupling, causing its cutoff angle to progressively increase. This transition is mathematically defined by the linear fitting equation θ_{cutoff} = 4.42n_0 - 2.84 ° (R^2 = 0.88498), which corresponds to a positive sensitivity θ_{TM} of +4.42 °/RIU. Both polarizations exhibit exceptional linearity, with correlation coefficients nearing unity, signifying that the measurement outcomes are highly dependable and consistent over the detection range. Although the absolute values of the sensitivities vary, the essential discovery is their contrasting signals. This unique differentiation in directional response establishes the physical basis for the ensuing differential detection technique, which is employed to enhance the overall sensor responsiveness and mitigate common-mode noise.

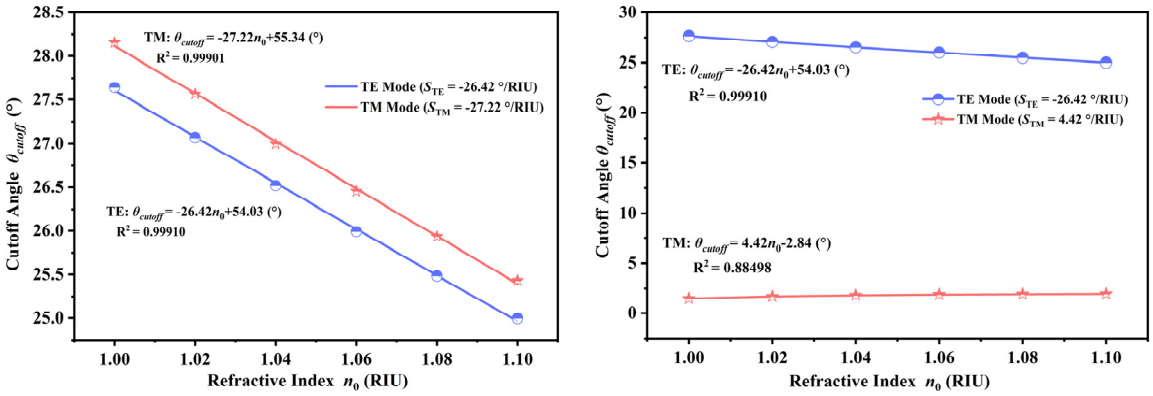

(**a**) (**b**)

Figure 6. Linear fitting of the angular sensitivity for the proposed sensor under distinct magnetic field configurations. (a) Dependence of the cutoff angle on the refractive index in the absence of an external magnetic field where *B* is 0 T, illustrating a synchronous blue-shift for both modes; (b) Dependence of the cutoff angle on the refractive index under the optimized magnetic field of 0.032 T. The numerical fitting results in figure 6(b) reveal the critical reverse-motion phenomenon, where the TE mode maintains a negative sensitivity of -26.42 °/RIU while the TM mode demonstrates a positive sensitivity of +4.42 °/RIU.

3.3. Differential Detection Strategy and Comprehensive Performance Evaluation

To enhance the sensing capability of the proposed structure, a differential detection scheme was adopted to quantify the sensing signal. Unlike conventional detection methods where the sensor response relies on a single resonance feature that is susceptible to environmental noise, the response in this system is determined by the absolute difference between the cutoff angles of the two orthogonal polarization modes. The differential angular shift, denoted as $\Delta\theta_{diff}$, represents the separation between the TE and TM cutoff edges. Consequently, the total differential sensitivity S_{diff} is theoretically defined as the absolute value of the disparity between the individual sensitivities.

$$S_{diff} = \left| S_{\mathrm{TE}} - S_{\mathrm{TM}} \right| \tag{10}$$

The effectiveness of this differential method relies significantly on the directional shifting patterns of the orthogonal modes. As illustrated in Figure 7, the differential angular shift exhibits completely distinct behaviors depending on the external magnetic field configuration. In the absence of an external magnetic field (B = 0T), both modes undergo synchronous blue-shifts. Because the algebraic signs of the individual sensitivities S_{TE} and S_{TM} are congruent, the differential computation inherently results in the subtraction of their magnitudes. Quantitative linear fitting verifies this limitation, yielding the equation $\Delta\theta$ = -0.8n_0 - 1.31 ° with R^2 of 0.9935. This corresponds to a negligible differential sensitivity of merely 0.8 °/RIU, offering minimal advantage over conventional single-mode detection. Conversely, the application of the external magnetic field (B = 0.033T) exploits the

© 2025 by the author(s). Distributed under a Creative Commons CC BY license.

Preprints.org (www.preprints.org) | NOT PEER-REVIEWED | Posted: 26 February 2026 doi:10.20944/preprints202602.1579.v1

unique reverse-motion characteristic, wherein the individual sensitivities exhibit opposing signs. Under this condition, subtracting the negative S_{TE} from the positive S_{TM} results in a constructive superposition of their absolute values. The linear fitting analysis for this magnetized state defines the relationship as $\Delta\theta = -30.84n_0 + 56.87$ ° ($R^2 = 0.9941$), which confirms a markedly enhanced differential sensitivity of 30.84 °/RIU. This exceptional value significantly surpasses the sensitivity attainable in the unmagnetized state, conclusively demonstrating that the magneto-optical effect is the principal driver for the overall performance enhancement of the proposed sensor.

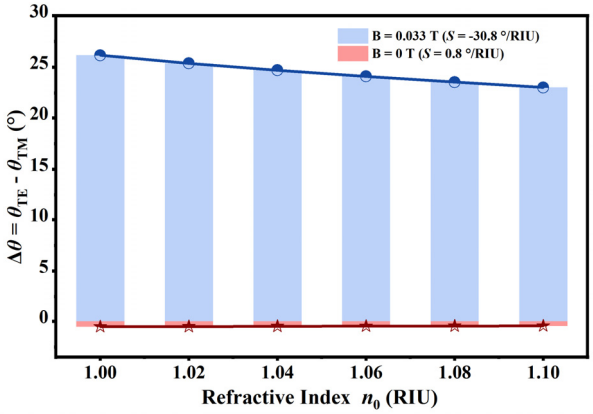

Figure 7. Comparative analysis of the differential angular shift as a function of the refractive index under distinct magnetic field configurations. (a) The response observed under the optimized magnetic field where $B = 0.033$ T exhibits a substantial differential sensitivity magnitude of 30.8 °/RIU. Conversely, the results obtained in the absence of an external magnetic field where $B = 0$ T yield a negligible sensitivity of 0.8 °/RIU. This distinct contrast demonstrates the significant sensitivity enhancement achieved through the proposed magneto-optical differential detection strategy.

A comprehensive evaluation of the realistic resolution limit was conducted by carefully assessing the *FWHM*, *FOM*, and 、 *LOD* of the sensor. As delineated in Section 3.1, the elevated *RC* of the structure guarantees an almost vertical band edge, which immediately correlates with a reduced *FWHM* of the derivative spectrum. This spectral acuity is essential for performance enhancement. The evaluation is fundamentally grounded in the optimized differential sensitivity, which demonstrates a robust linear response characterized by the equation $\Delta\theta = -49.090n_0 + 75.554$ ° with a correlation coefficient of $R^2 = 0.9979$. The *FOM* is defined as the ratio of sensitivity to *FWHM*. The proposed sensor attains remarkable figures of merit due to this enhanced differential sensitivity combined with the reduced *FWHM*. Figure 8(a) illustrates that the differential mode displays the highest *FOM* throughout the full detection range, markedly exceeding the individual TE and TM modes. This superior performance is quantitatively defined by the linear fitting equation $y = -2.575n_0 + 15.171$ /RIU with $R^2 = 0.8500$. Furthermore, the *LOD* is inversely related to the product of sensitivity and the quality factor, mathematically represented as the *FWHM* divided by twenty times the sensitivity. Figure 8(b) demonstrates that the differential mode achieves the optimal resolution capability. The linear regression for the differential *LOD* is described by $y = 0.000854n_0 - 0.000478$ RIU with an exceptional linearity of $R^2 = 0.9993$, ultimately reaching a minimal detection limit of roughly 4.18×10^{-4} RIU. This superior performance metric indicates that the sensor is capable of resolving extremely minute variations in refractive index, thereby validating the suitability of the proposed device for high-precision biosensing and gas detection applications.

© 2025 by the author(s). Distributed under a Creative Commons CC BY license.

Preprints.org (www.preprints.org) | NOT PEER-REVIEWED | Posted: 26 February 2026 doi:10.20944/preprints202602.1579.v1

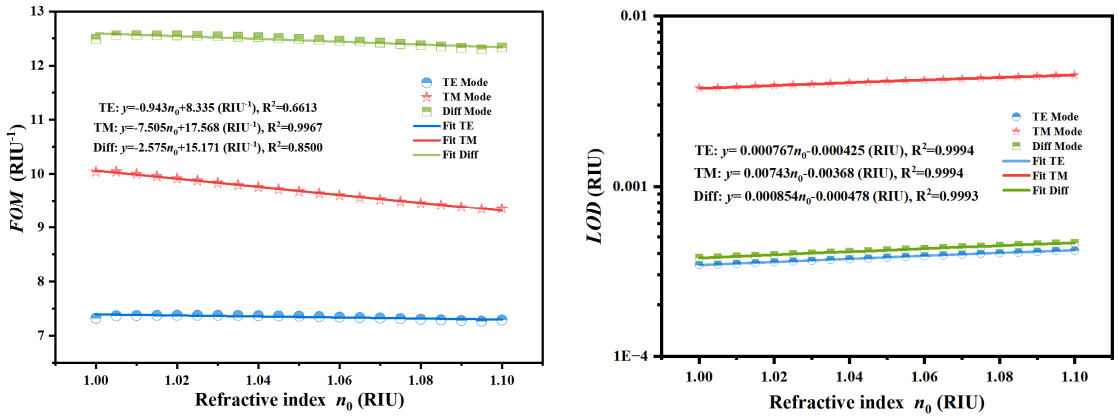

(**a**) (**b**)

Figure 8. Comprehensive performance evaluation of the MO-DPCS comparing TE, TM, and differential detection mode under the optimized magnetic field. (a) Calculated *FOM* as a function of refractive index, where the differential mode exhibits the highest values, confirming its superior spectral quality and sensitivity balance; (b) Calculated *DL* as a function of refractive index using a logarithmic scale, revealing that the differential mode achieves the lowest detection limit of approximately 4.18 × 10^{-4} RIU, demonstrating the enhanced capability in resolving minute refractive index variations.

To further highlight the practical superiority of the proposed MO-DPCS, Table 3 presents a comprehensive comparison with recently reported optical refractive index gas sensors. Conventional sensing designs often exhibit highly restricted detection ranges, thereby limiting their applicability to a narrow selection of target analytes. In contrast, the differential sensing architecture developed in this study provides an exceptionally broad detection range spanning from 1.000 to 1.100 RIU. Coupled with the ultra-low Limit of Detection established in the preceding analysis, this expansive range empowers the proposed sensor to effectively monitor a highly diverse array of critical industrial and hazardous gases. As detailed in the table, these include methane, carbon monoxide, sulfur dioxide, and various nitrogen oxides, whose refractive indices are notoriously close to that of atmospheric air. This comparison conclusively validates the versatility and engineering potential of the MO-DPCS for complex environmental and industrial monitoring scenarios.

Table 3. The proposed MO-DPCS for gas refractive index sensing is compared with the related researches.

Refs.	Detection range	Gas types
[25]	RI: 1.00026 ~ 1.00046 (RIU)	N_2O, CO_2
[66]	RI: 1.00 ~ 1.08 (RIU)	SO_x, NO_x, CO
[67]	RI: 1.000265 ~ 1.000407 (RIU)	Air, N_2, He, CO_2
Our work	RI: 1.000 ~ 1.100 (RIU)	CH_4 (n = 1.000444) CO (n = 1.000297) SO_2 (n = 1.000683) NO_x (n ≈ 1.0002 ~ 1.0008) Air (n = 1.000293) Industrial volatile gases (VOCs):Heavy chemical vapors(n ≈ 1.010 ~ 1.100)

3.4. Temperature Cross-Sensitivity and Environmental Stability Analysis

A major obstacle in the implementation of semiconductor-based photonic sensors is the inherent heat sensitivity of the materials involved. The permittivity of InSb is very responsive to temperature fluctuations, resulting in a refractive index alteration that may be indistinguishable from the signal produced by the target analyte. This effect, termed temperature cross-sensitivity, significantly undermines detection accuracy in real settings where thermal fluctuations are unavoidable,

© 2025 by the author(s). Distributed under a Creative Commons CC BY license.

Preprints.org (www.preprints.org) | NOT PEER-REVIEWED | Posted: 26 February 2026 doi:10.20944/preprints202602.1579.v1

potentially resulting in false positive results. The spectral response was examined throughout a temperature range of 274 K to 275 K to assess the robustness of the proposed device against external noise.

Figure 9(a) specifically illustrates the limitations of traditional single-mode detection. With a temperature rise of just 1 K, the cutoff angles for both TE and TM modes demonstrate a significant synchronous shift, transitioning from roughly +11° to -12°. The significant angular deviation over 20° suggests that even little thermal fluctuations may be misconstrued as considerable alterations in the refractive index of the target gas, hence compromising the reliability of single-mode measurements without stringent temperature stabilizing measures.

In contrast, the differential detection strategy effectively mitigates this issue by exploiting the common-mode nature of the thermal response. Since the temperature variation induces a similar kinematic shift in both polarization modes, the subtraction of the two cutoff angles inherently cancels out the majority of the thermal drift. The stability of the differential signal is presented in Figure 9(b). It is observed that the magnitude of the differential angular shift is confined within a narrow range of approximately 0.35° over the same temperature interval. Compared to the single-mode drift, the temperature cross-sensitivity is suppressed by nearly two orders of magnitude. This result confirms that the proposed differential sensor possesses a self-referencing capability, allowing it to distinguish the true refractive index signal from thermal noise and ensuring high measurement reliability in complex experimental conditions.

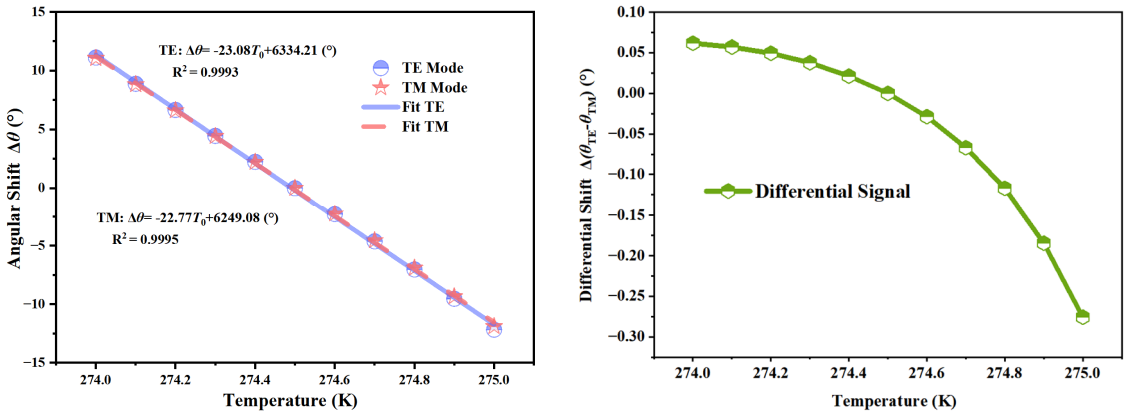

(a) (b)

Figure 9. Temperature cross-sensitivity analysis of the MO-DPCS over the range from 274 K to 275 K. (a) Angular drift of individual TE and TM modes, showing a substantial synchronous shift exceeding 20° due to the high thermal dependence of the InSb permittivity; (b) Variation of the differential signal under identical thermal conditions, revealing that the differential scheme effectively mitigates common-mode noise and restricts the drift to approximately 0.35°, demonstrating superior environmental stability.

4. Conclusion

The results presented in this study demonstrate that the integration of the magneto-optical effect with 1D PCs provides a robust mechanism for enhancing refractive index sensing performance, validating the working hypothesis that the non-reciprocal nature of magnetized InSb can be manipulated to induce opposing spectral shifts in orthogonal polarization modes. Crucially, the structural efficacy was maximized through the implementation of the MODA, which enabled the precise inverse design of layer thicknesses to achieve an optimal *RC* that manual tuning could not easily attain. While previous studies have predominantly focused on simple geometric optimization to narrow resonance linewidths, the approach utilized here synergizes algorithmic design with the external magnetic field as a new degree of freedom, enabling a transition from absolute angular detection to a differential scheme that amplifies sensitivity from a negligible 0.8 °/RIU to a substantial 30.8 °/RIU. Interpreting these findings in a broader context, the proposed MO-DPCS addresses the

© 2025 by the author(s). Distributed under a Creative Commons CC BY license.

Preprints.org (www.preprints.org) | NOT PEER-REVIEWED | Posted: 26 February 2026 doi:10.20944/preprints202602.1579.v1

critical challenge of environmental instability inherent to semiconductor-based sensing. Specifically, the differential strategy effectively converts the high thermal cross-sensitivity of InSb into a common-mode noise factor that is mathematically cancelled out, thereby ensuring high measurement reliability. Future research directions should focus on the experimental realization of the proposed structure via precision growth techniques such as molecular beam epitaxy, and potentially extending the concept to intelligent sensing systems where machine learning algorithms could further enhance real-time data demodulation and pattern recognition in miniaturized on-chip sensor arrays.

Author Contributions: J.Z.: Investigation, Data curation, Formal analysis, Writing—original draft, Visualization, Software, Validation. C.X.: Visualization. H.Z.: Conceptualization, Methodology, Supervision, Writing—review and editing. All authors have read and agreed to the published version of the manuscript.

Funding: This work was supported by the Open Research Program in China's State Key Laboratory of Millimeter Waves (Grant No. KN202502-15), Yangzhou Municipal-University Collaboration Special Program (Grant No. YZ2024233), and the National College Students Innovation and Entrepreneurship Training Program (Grant No. 202513989003G).

Institutional Review Board Statement: Not applicable.

Informed Consent Statement: Not applicable.

Data Availability Statement: Dataset available on request from the authors.

Acknowledgments: This work was supported by the College Student Innovation Training Program of Tongda College of Nanjing University of Posts and Telecommunications.

Conflicts of Interest: The authors declare no conflicts of interest.

References

1. Waleed, D.; Mustafa, S.H.; Mukhopadhyay, S.; Abdel-Hafez, M.F.; Jaradat, M.A.K.; Dias, K.R.; Arif, F.; Ahmed, J.I. An In-Pipe Leak Detection Robot With a Neural-Network-Based Leak Verification System. IEEE Sens. J. **2019**, 19, 1153–1165. https://doi.org/10.1109/JSEN.2018.2879248.
2. Jackson, R.B.; Down, A.; Phillips, N.G.; Ackley, R.C.; Cook, C.W.; Plata, D.L.; Zhao, K. Natural Gas Pipeline Leaks Across Washington, DC. Environ. Sci. Technol. **2014**, 48, 2051–2058. https://doi.org/10.1021/es404474x.
3. Wan, B.F.; Wang, Q.Y.; Peng, H.M.; Ye, H.N.; Zhang, H.F. A late-model optical biochemical sensor based on OTS for methane gas and glucose solution concentration detection. IEEE Sens. J. **2021**, 21, 21465–21472. https://doi.org/10.1109/JSEN.2021.3103548.
4. Zhao, Y.; Lei, M.; Liu, S.X.; Zhao, Q. Smart hydrogel-based optical fiber SPR sensor for pH measurements. Sens. Actuators, B **2018**, 261, 226–232. https://doi.org/https://doi.org/10.1016/j.snb.2018.01.120.
5. Sheng, G.; She, K.; Shan, Z.P.; Liu, E.X.; Peng, Y.C.; Liu, J.J. Topologically-protected dual-parameter Valley Hall photonic crystal sensor. Opt. Express **2025**, 33, 25558–25569. https://doi.org/10.1364/OE.562316.
6. Wilson, G.S.; Gifford, R. Biosensors for real-time in vivo measurements. Biosens. Bioelectron. **2005**, 20, 2388–2403. https://doi.org/https://doi.org/10.1016/j.bios.2004.12.003.
7. Samavati, Z.; Samavati, A.; Ismail, A.F.; Yahya, N.; Othman, M.H.D.; Rahman, M.A. Modified polymer optical fiber sensors for crude oil refractive index monitoring. J. Mater. Sci.: Mater. Electron. **2020**, 31, 12089–12100. https://doi.org/10.1007/s10854-020-03754-4.
8. Shakya, A.K.; Singh, S. Novel Merger of spectroscopy and refractive index sensing for modelling hyper sensitive hexa-slotted plasmonic sensor for transformer oil monitoring in near-infrared region. Opt. Quantum Electron. **2023**, 55, 764. https://doi.org/10.1007/s11082-023-05016-z.
9. Pulikottil, S.; Kasztelanic, R.; Stepniewski, G.; Baltuška, A.; Buczynski, R.; Bugár, I. Refractive index sensor based on the natural roughness of a directly fabricated D-shape fiber for biological and environmental monitoring purposes. Opt. Fiber Technol. **2024**, 88, 104036. https://doi.org/https://doi.org/10.1016/j.yofte.2024.104036.

© 2025 by the author(s). Distributed under a Creative Commons CC BY license.

Preprints.org (www.preprints.org) | NOT PEER-REVIEWED | Posted: 26 February 2026 doi:10.20944/preprints202602.1579.v1

10. Huang, C.H.; He, J.; Austin, E.; Seto, E.; Novosselov, I. Assessing the value of complex refractive index and particle density for calibration of low-cost particle matter sensor for size-resolved particle count and PM2.5 measurements. Plos One **2021**, 16, e0259745. https://doi.org/10.1371/journal.pone.0259745.
11. Butt, M.A.; Imran Akca, B.; Mateos, X. Integrated Photonic Biosensors: Enabling Next-Generation Lab-on-a-Chip Platforms. Nanomaterials **2025**, 15, 731. https://doi.org/https://doi.org/10.3390/nano15100731.
12. Fuentes Pérez, J.F.; Martínez Miguel, M.; García Vega, A.; Bravo Córdoba, F.J.; Sanz Ronda, F.J. Design and Initial Validation of an Infrared Beam-Break Fish Counter ('Fish Tracker') for Fish Passage Monitoring. Sensors **2025**, 25, 4112.
13. Karapateas, L.; Leonidas, E.; Meng, X.F.; Lai, Y.F.; Zhang, Y.; Willmott, J.R.; Hobbs, M.J. InAsSb Photodiode-Based Infrared Radiation Thermometer for the Investigation of Droplet Surface Temperature Dynamics Within an Enclosed Combustion Chamber. Sensors **2025**, 25, 5780. https://doi.org/https://doi.org/10.3390/s25185780.
14. Santos, J.L. Optical Sensors for Industry 4.0. IEEE J. Sel. Top. Quantum Electron. **2021**, 27, 1–11. https://doi.org/10.1109/JSTQE.2021.3078126.
15. Hu, P.; Xie, C.W.; Song, Q.J.; Chen, A.; Xiang, H.; Han, D.Z.; Zi, J. Bound states in the continuum based on the total internal reflection of Bloch waves. Natl. Sci. Rev. **2023**, 10, nwac043. https://doi.org/10.1093/nsr/nwac043.
16. Yablonovitch, E.; Gmitter, T.J. Photonic band structure: The face-centered-cubic case. Phys. Rev. Lett. **1989**, 63, 1950–1953. https://doi.org/10.1103/PhysRevLett.63.1950.
17. Nishijima, Y.; Ueno, K.; Juodkazis, S.; Mizeikis, V.; Misawa, H.; Tanimura, T.; Maeda, K. Inverse silica opal photonic crystals for optical sensing applications. Opt. Express **2007**, 15, 12979–12988. https://doi.org/10.1364/OE.15.012979.
18. Viphavakit, C.; Keeffe, S.O.; Yang, M.; Andersson-Engels, S.; Lewis, E. Gold Enhanced Hemoglobin Interaction in a Fabry–Pérot Based Optical Fiber Sensor for Measurement of Blood Refractive Index. J. Lightwave Technol. **2018**, 36, 1118–1124. https://doi.org/10.1109/JLT.2017.2782078.
19. Li, W.W.; Chen, W.P.; Wang, D.N.; Wang, Z.K.; Xu, B. Fiber inline Mach-Zehnder interferometer based on femtosecond laser inscribed waveguides. Opt. Lett. **2017**, 42, 4438–4441. https://doi.org/10.1364/OL.42.004438.
20. Ivanov, I.; Skryshevsky, V.; Belarouci, A. Porous silicon photonic crystal-based interferometric chemical sensor. Opt. Express **2025**, 33, 40891–40901. https://doi.org/10.1364/OE.549742.
21. Ullah, S.; Chen, H.L.; Guo, P.X.; Song, M.S.; Zhang, S.; Hu, L.C.; Li, S.G. A Highly Sensitive D-Shaped PCF-SPR Sensor for Refractive Index and Temperature Detection. Sensors **2024**, 24, 5582. https://doi.org/https://doi.org/10.3390/s24175582.
22. Ehiabhili, J.; Prabhu, R.; Kannan, S. Design and Numerical Analysis of an Ultra-Sensitive π-Configuration Fibre Optic-Based SPR Sensor: Dual Plasmonic Enhancement for Low-Refractive-Index Biomolecular Detection. Photonics **2026**, 13, 147.
23. Hasan, A.; Chowdhury, A.; Adib, A.; Das, D.; Ferdous, A.H.M.I.; Mitul, A.F.; Akhtar, J.; Reja, M.I. An Ultra-Sensitive Bimetallic-Coated PCF-Based Surface Plasmon Resonance Sensor for Waterborne Pathogen Detection. Photonics **2025**, 12, 1240.
24. Liang, G.L.; Zhao, Z.J.; Wei, Y.; Liu, K.P.; Hou, W.Q.; Duan, Y.X. Plasma enhanced label-free immunoassay for alpha-fetoprotein based on a U-bend fiber-optic LSPR biosensor. RSC Advances **2015**, 5, 23990–23998. https://doi.org/10.1039/C5RA02910D.
25. Zaky, Z.A.; Ahmed, A.M.; Shalaby, A.S.; Aly, A.H. Refractive index gas sensor based on the Tamm state in a one-dimensional photonic crystal: Theoretical optimisation. Sci. Rep. **2020**, 10, 9736. https://doi.org/10.1038/s41598-020-66427-6.
26. Shokrekhodaei, M.; Cistola, D.P.; Roberts, R.C.; Quinones, S. Non-Invasive Glucose Monitoring Using Optical Sensor and Machine Learning Techniques for Diabetes Applications. IEEE Access **2021**, 9, 73029–73045. https://doi.org/10.1109/ACCESS.2021.3079182.
27. Zhou, G.L.; Li, L.Y.; Zhou, Y.; Chen, X.Y. Measurement Error Analysis of Seawater Refractive Index: A Measurement Sensor Based on a Position-Sensitive Detector. Sensors **2024**, 24, 4564. https://doi.org/https://doi.org/10.3390/s24144564.

© 2025 by the author(s). Distributed under a Creative Commons CC BY license.

Preprints.org (www.preprints.org) | NOT PEER-REVIEWED | Posted: 26 February 2026 doi:10.20944/preprints202602.1579.v1

28. Shen, W.M.; Norrie, D.H. Agent-Based Systems for Intelligent Manufacturing: A State-of-the-Art Survey. Knowl. Inf. Syst. **1999**, 1, 129–156. https://doi.org/10.1007/BF03325096.
29. Tavana, S.; Bahadori Haghighi, S.; Ye, W.N. Tunable and ultra-narrowband multifunctional terahertz devices using anisotropic graphene based hyperbolic metamaterials. Sci. Rep. **2024**, 14, 31303. https://doi.org/https://doi.org/10.1038/s41598-024-82763-3.
30. Tian, H.S.; Wang, H.B.; Zhang, J.K.; Sun, G. Controllable Goos-Hänchen Shift in Photonic Crystal Heterostructure Containing Anisotropic Graphene. Coatings **2024**, 14, 1092. https://doi.org/10.3390/coatings14091092.
31. Qing, Y.M.; Ma, H.F.; Wu, L.W.; Cui, T.J. Manipulating the light-matter interaction in a topological photonic crystal heterostructure. Opt. Express **2020**, 28, 34904–34915. https://doi.org/10.1364/oe.405434.
32. Yablonovitch, E. Inhibited Spontaneous Emission in Solid-State Physics and Electronics. Phys. Rev. Lett. **1987**, 58, 2059–2062. https://doi.org/10.1103/PhysRevLett.58.2059.
33. Qi, X.; Wu, J.J.; Wu, F.; Ren, M.N.; Wei, Q.; Guo, Z.W.; Jiang, H.T.; Chen, Y.G.; Yang, Y.P.; Chen, H. Topologically enabled giant angle-insensitive Goos-Hänchen shift by tunable merging bound states in the continuum of a quasiflat band. Phys. Rev. B **2024**, 110, 035420. https://doi.org/10.1103/PhysRevB.110.035420.
34. Li, M.Y.; Luo, Z.W.; Zhou, X.; Zhang, Z.X.; Wang, M.M.; Chen, B.; Xiao, L.; Duan, Y.X.; Li, L.Y. Core–Shell Structure of AuNPs@PDMS Nanoparticle-Modified Silver Film on Bent Optical Fiber to Design a SPR Sensor for Synchronous Detection of Temperature and Refractive Index. Plasmonics **2025**, 20, 10547–10558. https://doi.org/10.1007/s11468-025-03139-5.
35. Dong, R.Y.; Sui, J.Y.; Li, Z.J.; Zhang, H.F. The terahertz isolator and switch based on the nonreciprocal feature of magnetized InSb layered photonic structure. Opt. Laser Technol. **2024**, 169, 110004. https://doi.org/https://doi.org/10.1016/j.optlastec.2023.110004.
36. Li, C.Y.; Xie, Y.J.; Wu, P.Y.; Chen, S. Nonreciprocal Terahertz Propagation via InSb Topological Photonic Crystals. Adv. Photonics Res. **2026**, 7, e202500253. https://doi.org/https://doi.org/10.1002/adpr.202500253.
37. Tan, Z.Y.; Fan, F.; Dong, X.P.; Cheng, J.R.; Chang, S.J. Nonreciprocal terahertz beam steering based on magneto-optic metagratings. Sci. Rep. **2019**, 9, 20210. https://doi.org/10.1038/s41598-019-56789-x.
38. Wan, B.F.; Xu, Y.; Zhou, Z.W.; Zhang, D.; Zhang, H.F. Theoretical Investigation of a Sensor Based on One-Dimensional Photonic Crystals to Measure Four Physical Quantities. IEEE Sens. J. **2021**, 21, 2846–2853. https://doi.org/10.1109/JSEN.2020.3027759.
39. Suzuki, R. Fabrication of a porous SiO_2 thin film with an ultralow refractive index for anti-reflective coatings. J. Sol-Gel Sci. Technol. **2023**, 106, 860–868. https://doi.org/10.1007/s10971-023-06108-8.
40. Wu, Y.H.; Shang, Z.H.; Li, Z.R.; Zhu, W.L.; Nie, L.F.; Liu, J.C. Porous SiO_2 antireflection film with high UV resistance. Opt. Mater. **2024**, 153, 115603. https://doi.org/https://doi.org/10.1016/j.optmat.2024.115603.
41. Kim, J.; Kim, J.Y.; Kim, J.; Hyeong, Y.; Neseli, B.; You, J.B.; Shim, J.; Shin, J.; Park, H.H.; Kurt, H. Inverse design of nanophotonic devices enabled by optimization algorithms and deep learning: recent achievements and future prospects. Nanophotonics **2025**, 14, 121–151. https://doi.org/doi:10.1515/nanoph-2024-0536.
42. Yang, D.; Huang, J.; Xu, B.; Lv, G.; Li, Y.J.; Cheng, T.L. Design of high-performance photonic crystal fiber polarization filter by Grey Wolf Optimizer with convolutional neural network. Optik **2023**, 283, 170925. https://doi.org/https://doi.org/10.1016/j.ijleo.2023.170925.
43. Sebek, M.; Thanh, N.T.K.; Su, X.D.; Teng, J.H. A Genetic Algorithm for Universal Optimization of Ultrasensitive Surface Plasmon Resonance Sensors with 2D Materials. ACS Omega **2023**, 8, 20792–20800. https://doi.org/10.1021/acsomega.3c01387.
44. Mirjalili, S. Dragonfly algorithm: a new meta-heuristic optimization technique for solving single-objective, discrete, and multi-objective problems. Neural Comput. Appl. **2016**, 27, 1053–1073. https://doi.org/10.1007/s00521-015-1920-1.
45. Rodríguez Suné, L.; Scalora, M.; Johnson, A.S.; Cojocaru, C.; Akozbek, N.; Coppens, Z.J.; Perez Salinas, D.; Wall, S.; Trull, J. Study of second and third harmonic generation from an indium tin oxide nanolayer: Influence of nonlocal effects and hot electrons. APL Photonics **2020**, 5. https://doi.org/10.1063/1.5129627.

© 2025 by the author(s). Distributed under a Creative Commons CC BY license.

Preprints.org (www.preprints.org) | NOT PEER-REVIEWED | Posted: 26 February 2026 doi:10.20944/preprints202602.1579.v1

46. Moras, A.L.; Silva, V.; Souza, M.C.M.M.; Cirino, G.A.; Zuben, A.A.G.V.; Barea, L.A.M.; Frateschi, N.C. Integrated Photonic Platform for Robust Differential Refractive Index Sensor. IEEE Photonics J. **2020**, 12, 1–10. https://doi.org/10.1109/JPHOT.2020.3024856.
47. Yang, Q.; Gao, L.X.; Zou, C.W.; Xie, W.; Tian, C.X.; Wang, Z.S.; Liang, F.; Ke, Y.H.; Zhou, X.M.; Li, S.Q. Differential Refractive Index Sensor Based on Coupled Plasmon Waveguide Resonance in the C-Band. Sensors **2021**, 21, 7984. https://doi.org/https://doi.org/10.3390/s21237984.
48. Wang, H.; Luo, J.; Dai, W.; Chen, S.; Fu, H. A Differential Intensity-Modulated Refractive Index Sensor Using a Droplet-Like Fiber Cascaded With FBGs. J. Lightwave Technol. **2022**, 40, 3098–3103. https://doi.org/10.1109/JLT.2022.3148189.
49. Mathew, J.; Schneller, O.; Polyzos, D.; Havermann, D.; Carter, R.M.; MacPherson, W.N.; Hand, D.P.; Maier, R.R.J. In-Fiber Fabry–Perot Cavity Sensor for High-Temperature Applications. J. Lightwave Technol. **2015**, 33, 2419–2425. https://doi.org/10.1109/JLT.2015.2397936.
50. Wan, B.F.; Ye, H.N.; Zhang, H.F. Multi-channel angular selective window based on the epsilon-near-zero features of YaBa2Cu3O7 material and photonic crystals ceramic structure of extremely small dispersion edge regions. Ceram. Int. **2023**, 49, 34814–34825. https://doi.org/https://doi.org/10.1016/j.ceramint.2023.08.155.
51. Shayegan, K.J.; Biswas, S.; Zhao, B.; Fan, S.H.; Atwater, H.A. Direct observation of the violation of Kirchhoff's law of thermal radiation. Nat. Photonics **2023**, 17, 891–896. https://doi.org/https://doi.org/10.1038/s41566-023-01261-6.
52. Ali, S.; Stanca, S.E.; Vegesna, S.V.; Schmidl, G.; Diegel, M.; Dellith, J.; Müller, R.; Wondraczek, K.; Plentz, J.; Krüger, H. Indium-tin-oxide thin films with real-epsilon-near-zero properties. Phys. B Condens. Matter **2025**, 417652. https://doi.org/https://doi.org/10.1016/j.physb.2025.417652.
53. Huang, X.J.; Yang, H.L.; Wang, D.Q.; Yu, S.Q.; Lou, Y.C.; Guo, L. Calculations of a wideband metamaterial absorber using equivalent medium theory. J. Phys. D: Appl. Phys. **2016**, 49, 325101. https://doi.org/10.1088/0022-3727/49/32/325101.
54. Wang, T.; Chen, G.; Zhu, J.H.; Gong, H.; Zhang, L.M.; Wu, H.J. Deep understanding of impedance matching and quarter wavelength theory in electromagnetic wave absorption. J. Colloid Interface Sci. **2021**, 595, 1–5. https://doi.org/https://doi.org/10.1016/j.jcis.2021.03.132.
55. Liang, Y.; Pakniyat, S.; Xiang, Y.x.; Shi, F.; Hanson, G.W.; Cen, C. Temperature-dependent transverse-field magneto-plasmons properties in InSb. Opt. Mater. **2021**, 112, 110831. https://doi.org/https://doi.org/10.1016/j.optmat.2021.110831.
56. He, X.F.; Zhang, H.F. Absorption and polarization based on metastructures: a review. Phys. Chem. Chem. Phys. **2025**, 27, 25720–25742. https://doi.org/10.1039/D5CP03307A.
57. Dai, X.Y.; Xiang, Y.J.; Wen, S.C.; He, H.Y. Thermally tunable and omnidirectional terahertz photonic bandgap in the one-dimensional photonic crystals containing semiconductor InSb. J. Appl. Phys. **2011**, 109. https://doi.org/10.1063/1.3549834.
58. Wan, B.F.; Ye, H.N.; Zhang, H.F. Ultra-Wideband Polarization Insensitive Angle Filter Based on ENZ Characteristics and Dynamic Antireflection Structures. Photonics **2022**, 9, 854. https://doi.org/https://doi.org/10.3390/photonics9110854.
59. Qi, L.; Yang, Z.; Lan, F.; Gao, X.; Shi, Z. Properties of obliquely incident electromagnetic wave in one-dimensional magnetized plasma photonic crystals. Phys. Plasmas **2010**, 17. https://doi.org/10.1063/1.3360296.
60. Iizuka, H.; Engheta, N.; Sugiura, S. Extremely small wavevector regime in a one-dimensional photonic crystal heterostructure for angular transmission filtering. Opt. Lett. **2016**, 41, 3829–3832. https://doi.org/10.1364/ol.41.003829.
61. Aly, A.; Abdel Ghany, S.E.S.; Kamal, B.; D, V. Theoretical studies of hybrid multifunctional $YaBa_2Cu_3O_7$ photonic crystals within visible and infra-red regions. Ceram. Int. **2019**, 46. https://doi.org/10.1016/j.ceramint.2019.08.270.
62. Hu, P.; Xie, C.W.; Song, Q.J.; Chen, A.; Xiang, H.; Han, D.Z.; Zi, J. Bound states in the continuum based on the total internal reflection of Bloch waves. Natl. Sci. Rev. **2022**, 10. https://doi.org/10.1093/nsr/nwac043.

© 2025 by the author(s). Distributed under a Creative Commons CC BY license.

Preprints.org (www.preprints.org) | NOT PEER-REVIEWED | Posted: 26 February 2026 doi:10.20944/preprints202602.1579.v1

63. Notomi, M. Theory of light propagation in strongly modulated photonic crystals: Refractionlike behavior in the vicinity of the photonic band gap. Phys. Rev. B **2000**, 62, 10696. https://doi.org/https://doi.org/10.1103/PhysRevB.62.10696.
64. Li, Z.Y.; Gu, B.Y.; Yang, G.Z. Large absolute band gap in 2D anisotropic photonic crystals. Phys. Rev. Lett. **1998**, 81, 2574. https://doi.org/https://doi.org/10.1103/PhysRevLett.81.2574.
65. Cheng, R.; Chrostowski, L. Apodization of Silicon Integrated Bragg Gratings Through Periodic Phase Modulation. IEEE J. Sel. Top. Quantum Electron. **2020**, 26, 1–15. https://doi.org/10.1109/JSTQE.2019.2929698.
66. Sharif, V.; Saberi, H.; Pakarzadeh, H. Designing a terahertz optical sensor based on helically twisted photonic crystal fiber for toxic gas sensing. Sci. Rep. **2025**, 15, 2268. https://doi.org/10.1038/s41598-024-82704-0.
67. Mohebbi, M. Refractive index sensing of gases based on a one-dimensional photonic crystal nanocavity. J. Sens. Sens. Syst. **2015**, 4, 209–215. https://doi.org/10.5194/jsss-4-209-2015.

Disclaimer/Publisher's Note: The statements, opinions and data contained in all publications are solely those of the individual author(s) and contributor(s) and not of MDPI and/or the editor(s). MDPI and/or the editor(s) disclaim responsibility for any injury to people or property resulting from any ideas, methods, instructions or products referred to in the content.

© 2025 by the author(s). Distributed under a Creative Commons CC BY license.